Check for updates

ADVANCED MATERIALS TECHNOLOGIES
www.advmattechnol.de

A Hydrophilic Hollow Microneedle Platform for Sampling Interstitial Fluid and On-Site Biomarker Detection

*Taher Abbasiasl, Sevgi Sarıca, Umut Can Yener, Emel Yilgor, Iskender Yilgor, Hatice Ceylan Koydemir, Ece Öztürk, and Levent Beker**

Minimally invasive health monitoring is crucial for advancing personalized medicine, and microneedle-based platforms have emerged as a promising tool for collecting dermal interstitial fluid (ISF) in a pain-free and easy-to-use manner. ISF provides a rich source of biomarkers, potentially replacing traditional blood-based diagnostics. In this study, a superhydrophilic hollow microneedle patch capable of continuous ISF extraction and on-patch biomarker detection is presented. Utilizing high-precision projection micro-stereolithography, biocompatible, polymeric multichannel hollow microneedles (HMN) with tip diameters of 5–10 µm, demonstrating excellent mechanical performance under compressive, shear, and penetration forces is fabricated. Wettability of HMN is dramatically enhanced by depositing a thin silicon oxide layer, which accelerates ISF extraction and enables prolonged and effective sampling. In vitro and ex vivo ISF extraction experiments are performed to investigate the effect of hydrophilicity, microchannel count, and microneedle height on liquid uptake. By integrating urea and pH colorimetric assays into the microneedle platform, direct, quantitative analysis of biomarkers from the sampled liquid is achieved. This all-in-one platform, combining superhydrophilic 3D-printed hollow microneedles and colorimetric sensing capabilities, represents a significant advancement toward the design and production of continuous, minimally invasive health monitoring devices.

1. Introduction

Recent technological advancements have significantly transformed the health sector, particularly in the development of wearable health monitoring devices.[1,2] Despite these advancements, diagnosis and monitoring mainly rely on blood analysis for biomolecular markers, whereas transdermal biosensing offers the potential to revolutionize healthcare by enabling real-time and continuous monitoring of key biomarkers in bodily fluids.[3,4] Dermal interstitial fluid (ISF), originating from transcapillary blood exchange and constituting ≈75% of extracellular fluid, shares a similar composition with blood. Moreover, ISF is the most abundant accessible fluid in the body and shares a high degree of biomarkers with plasma, thus holding a great potential to replace current blood-based diagnostic techniques.[5,6]

Although ISF is readily accessible throughout the skin, sampling it remains

T. Abbasiasl, L. Beker
Department of Biomedical Sciences and Engineering
Koç University
Rumelifeneri Yolu, Sarıyer, Istanbul 34450, Turkey
E-mail: lbeker@ku.edu.tr

S. Sarıca
Department of Cellular and Molecular Medicine
Koç University
Rumelifeneri Yolu, Sarıyer, Istanbul 34450, Turkey

S. Sarıca, E. Öztürk, L. Beker
Koç University Research Center for Translational Research (KUTTAM)
Koç University
Rumelifeneri Yolu, Sarıyer, Istanbul 34450, Turkey

U. C. Yener, L. Beker
Department of Mechanical Engineering
Koç University
Rumelifeneri Yolu, Sarıyer, Istanbul 34450, Turkey

E. Yilgor, I. Yilgor
Department of Chemistry
Koç University
Rumelifeneri Yolu, Sarıyer, Istanbul 34450, Turkey

H. Ceylan Koydemir
Department of Biomedical Engineering
Texas A&M University
College Station, TX 77843, USA

E. Öztürk
Department of Medical Biology, School of Medicine
Koç University
Rumelifeneri Yolu, Sarıyer, Istanbul 34450, Turkey

L. Beker
Nanofabrication and Nanocharacterization Center for Scientific and Technological Advanced Research (n2Star)
Koç University
Rumelifeneri Yolu, Sarıyer, Istanbul 34450, Turkey

H. Ceylan Koydemir
Center for Remote Health Technologies and Systems
Texas A&M Engineering Experiment Station
TX, Istanbul 77843, USA

The ORCID identification number(s) for the author(s) of this article can be found under https://doi.org/10.1002/admt.202500891

© 2025 The Author(s). Advanced Materials Technologies published by Wiley-VCH GmbH. This is an open access article under the terms of the Creative Commons Attribution License, which permits use, distribution and reproduction in any medium, provided the original work is properly cited.

DOI: 10.1002/admt.202500891

challenging due to its low volume in the dermis. Assuming 40% of the dermis consists of ISF, only 120 μL cm^{-2} is accessible in the thickest regions of the dermis. Furthermore, another significant constraint to ISF extraction is its slow natural replenishment rate within the dermis. The high hydraulic resistance of the dermis further hinders fluid flow. It takes nearly 30 h for the dermal ISF content to fully refresh.[3,7] Several challenges associated with conventional ISF collection techniques remain unaddressed. For instance, ISF sampling using suction blisters and biopsy punches can cause discomfort, irritation, and skin damage, and the collected fluid may be contaminated with injury-related biomarkers, leading to distorted analyte concentrations.[8,9] Microdialysis requires several h to perform, causes tissue damage, and the membrane's permeability limits the range of collected analytes.[10] Reverse iontophoresis can only collect small molecules and requires frequent calibration. ISF dilution, considerable lag time, and contamination by sweat are other drawbacks of this method.[6] Therefore, there is a demand for new, simple techniques capable of rapidly extracting adequate amounts of ISF (≥1 μL, sufficient for many assays), while minimizing tissue damage.

Microneedles—micron-sized needle arrays with lengths typically ranging from 50–2000 μm— [11] have garnered significant attention in various biomedical applications, including biomarker sensing, drug delivery, and tissue sampling.[12] Due to their short length compared to hypodermic needles used in commercial continuous glucose monitoring devices (CGMs) (5–13 mm),[13] microneedles can pierce the stratum corneum and reach the dermis layer without stimulating dermal nerves. Despite extensive research on implementing microneedles for drug and vaccine delivery and in situ biomarker monitoring,[14–17] studies employing extracted ISF for medical applications remain scarce.[3,6] Recently, hydrogel-forming microneedles have been widely used for ISF extraction owing to their superior water absorption and swelling capabilities.[18–21] Although they extract ISF more rapidly than other techniques, hydrogel microneedles become saturated upon reaching their maximum absorption capacity, rendering them less suited for continuous, long-term health monitoring. In addition, some metabolites become entrapped in the hydrogel matrix, necessitating cumbersome extraction processes for analysis. Hollow and/or porous microneedles are alternative types that leverage capillary forces for ISF extraction.[22–24] Some studies have integrated vacuum systems with hollow microneedles to enhance their ISF extraction capability.[25–27] Hollow microneedles have demonstrated the ability to extract adequate amounts of ISF to enable various biomarker sensing techniques, including electrochemical, colorimetric, and optical methods.[27–29] However, since most hollow microneedles are fabricated from polymeric materials (e.g., via 3D printing), the hydrophobic nature of the needle bores necessitates integrating a vacuum system to initiate and maintain a continuous flow.[18] Enhancing the wettability of microneedle channels to promote liquid movement through improved capillary action is highly desirable. Increasing the hydrophilicity of hollow microneedles can obviate the need for external driving forces for ISF extraction, thereby enabling ISF sampling using a single microneedle patch. This advancement will support the implementation of microneedle-based ISF extraction across a wide range of applications, including clinical research (such as cytokine analysis for dermatological studies), pharmaceutical advancements, cosmetics, and continuous health monitoring.

In recent years, the accuracy and flexibility of 3D printing technology have enabled the fabrication of microneedles with complex structures,[30,31] reduced tip sizes,[32,33] and higher needle densities. In particular, hollow microneedles have benefited from 3D printing advancements due to easy fabrication, increased number of channels per needle, and customizable channel designs.[34] Extensive research has focused on integrating 3D-printed hollow microneedles into wearable health monitoring devices. Among various 3D printing techniques, (e.g., fused deposition modelling, stereolithography, selective laser sintering, digital light processing) several studies have used projection micro-stereolithography (PμSL) to fabricate robust and intricate microneedles for wearable platforms.[26,35,36] However, employing these microneedles for effective ISF extraction from humans without external stimuli such as vacuum remains an unmet challenge. Therefore, developing a hollow microneedle patch that can passively extract adequate amounts of ISF from live tissues could offer significant advantages.

In this study, we developed a 3D-printed hollow microneedle patch with superhydrophilic microchannels to effectively collect dermal ISF for continuous biomarker sensing. Biocompatible conical microneedles with various designs and dimensions are easily fabricated using PμSL. Depositing a hydrophilic silicone oxide (SiO_2) layer on the microchannel surface significantly enhances the wettability of microneedles, resulting in drastically improved capillary forces that enables passive liquid uptake. The 3D-printed microneedles exhibit excellent mechanical performance against compressive, shear, and penetration forces. The superhydrophilic coating on the channel walls reduces the water contact angle from 72 to 9°, creating a strong capillary action that extracts ISF from agarose gel without any external force and enhances liquid uptake from rat skin samples. We perform a parametric study to investigate the effect of different microneedle designs on liquid uptake. Finally, we demonstrate the applicability of the developed microneedle patch by integrating it with a colorimetric assay for urea and pH sensing. The proposed microneedle device exhibits excellent mechanical and liquid uptake performance, offering a practical ISF extraction approach that eliminates the need for external forces in health monitoring devices. This approach will be particularly beneficial for polymer-based microneedles, whose natural hydrophobicity acts against ISF extraction.

2. Results and Discussion

2.1. Design and Fabrication of the Microneedle Patches

The ISF sampling approach in this study relies on microneedle arrays with through microchannels that penetrate the dermis layer and transport dermal ISF to the integrated microfluidic module. The microneedle patch was fabricated employing highly reproducible PμSL technology (**Figure 1a,b**). This technique utilizes a three-dimensional computer-aided design for rapid photopolymerization of liquid resin using flashes of UV light. Each microneedle patch contains 100 (10 × 10 array) conical microneedles within a patch area of 16 × 16 mm^2 (Figure 1c). Detailed morphological characterization was

© 2025 The Author(s). Advanced Materials Technologies published by Wiley-VCH GmbH

2365709x, 2025, 22, Downloaded from https://advanced.onlinelibrary.wiley.com/doi/10.1002/admt.202500891 by Koc University, Wiley Online Library on [07/12/2025]. See the Terms and Conditions (https://onlinelibrary.wiley.com/terms-and-conditions) on Wiley Online Library for rules of use; OA articles are governed by the applicable Creative Commons License

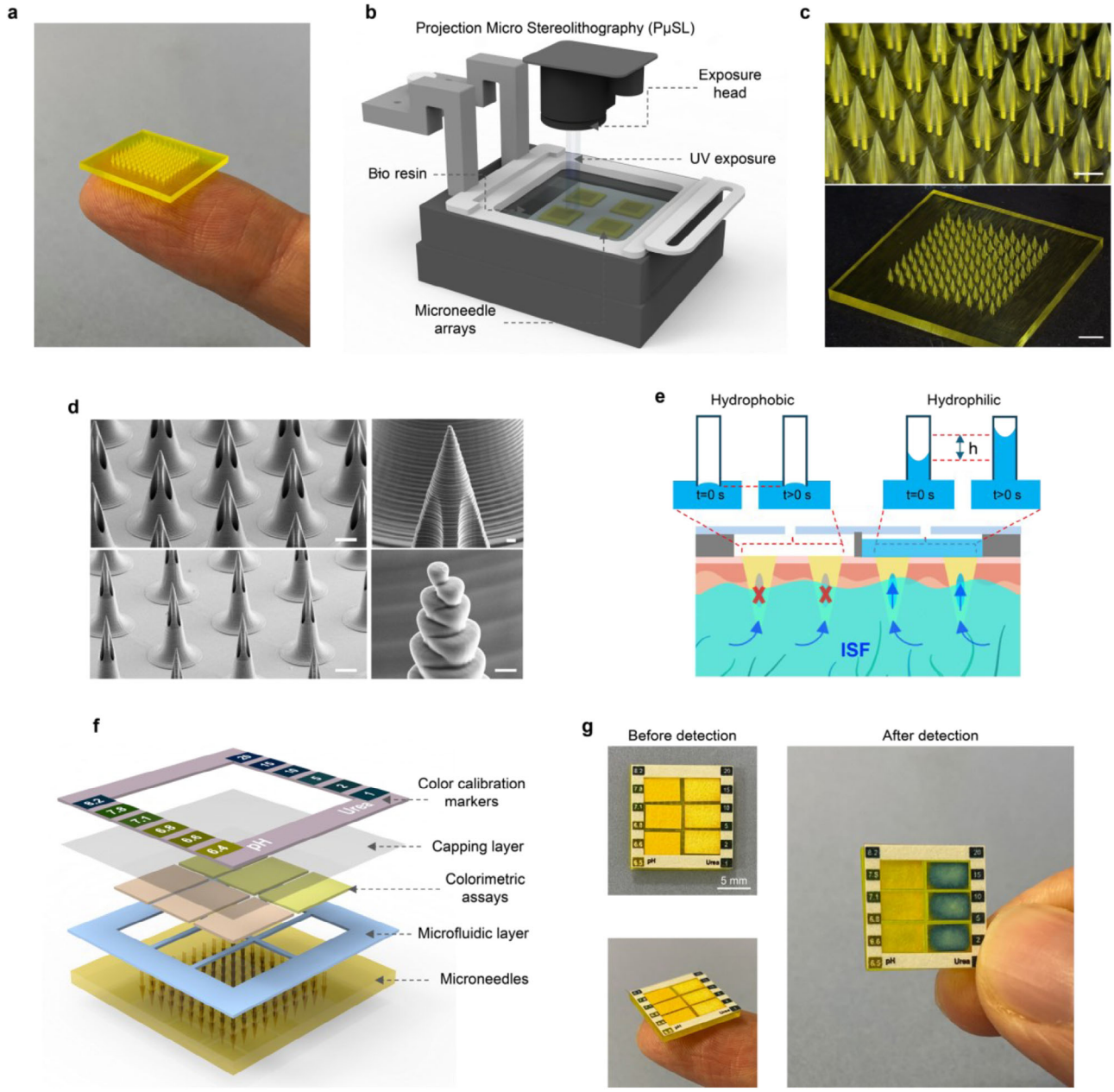


Figure 1. Illustration of 3D-printed microneedles for extraction and colorimetric sensing of dermal ISF. a) Image of the 3D-printed microneedles prepared by PμSL. b) Schematic representation of the fabrication process of the microneedles by PμSL. c) Representative microscopy images of a microneedle patch with two built-in microchannels per needle (MN-2). Scale bar, top: 500 μm, bottom: 2 mm. d) SEM images of 3D-printed microneedles. The bottom right-hand side image displays the obtained diameter of ≈5 μm for microneedle tips (top: MN-3 and bottom: MN-5). Scale bars, left: 200 μm, right: 5 μm. e) Schematic illustration of the ISF collection using 3D-printed microneedles. f) Exploded view illustration of the different layers of the colorimetric patch. g) Top and side view of the assembled colorimetric patch for urea and pH detection (left side) and color change of the colorimetric assays (right side). Detailed information about the dimensions of the microneedles is provided in Table 1.

performed by scanning electron microscopy (SEM) (Figure 1d). The SEM images showed that the fabricated microneedles had a tip diameter of ≈5 μm, comparable to the tip radii of microneedles prepared using photolithography-based techniques.[37,38] Image analysis of the top-view SEM images of the microchannels revealed a printing accuracy of ≈85% (Figures S1,S2, Supporting Information).

Figure 1e schematically illustrates the ISF extraction process using the 3D-printed hollow microneedles. Due to the hydrophobic nature of the as-printed microneedles, no liquid uptake is observed due to the absence of capillary flow (Note S2, Supporting Information). However, enhancing the wettability of the microchannels induces capillary rise inside the channels, which assists in ISF extraction. As shown in Figure 1e, while there is no

© 2025 The Author(s). Advanced Materials Technologies published by Wiley-VCH GmbH

2365709x, 2025, 22, Downloaded from https://advanced.onlinelibrary.wiley.com/doi/10.1002/admt.202500891 by Koc University, Wiley Online Library on [07/12/2025]. See the Terms and Conditions (https://onlinelibrary.wiley.com/terms-and-conditions) on Wiley Online Library for rules of use; OA articles are governed by the applicable Creative Commons License

Table 1. Design of different microneedle patches used in this study.

Microneedle label	Shape	Height [mm]	Base diameter [μm]	Center to center [mm]	Number of microchannels	Microchannel diameter [μm]
MN-1	Conical	1	500	1	0	–
MN-2	Conical	1	500	1	2	100
MN-3	Conical	1	500	1	4	100
MN-4	Conical	1	300	1	2	50
MN-5	Conical	1	300	1	4	50
MN-6	Conical	1.25	500	1	2	100
MN-7	Conical	1.5	500	1	2	100

capillary rise in hydrophobic microchannels, the hydrophilic microchannels exhibit liquid uptake capability due to enhanced capillary action. In this study, the microneedle patch was designed as a two-component system consisting of the 3D-printed hollow microneedles (which create the micropores in the skin for ISF extraction from the dermis) and a microfluidic layer (which serves as the ISF collection chamber).

The microfluidic chambers contain paper-based colorimetric assays for detecting urea and pH in the extracted ISF. An exploded view of the different components of the multilayered colorimetric patch is illustrated in Figure 1f. Upon extraction through superhydrophilic microchannels in the microneedle patch, the extracted liquid is collected in the microfluidic chambers (constructed using a 170 μm-thick double-sided tape) and comes into contact with the embedded colorimetric assays for urea and pH sensing. Multiple microfluidic chambers are included for each biomarker to increase the detection accuracy. The microfluidic layer is enclosed by a thin, transparent capping layer. Finally, a layer containing color reference markers is attached as the top layer to assist with quantitative analysis of the images. Figure 1g shows representative images of the final microneedle patch with integrated colorimetric assays before and after the color changes resulting from urea and pH sensing.

2.2. Mechanical Performance of the 3D-Printed Microneedles

To determine whether the as-fabricated microneedles can tolerate the required compressive and shear forces to penetrate the skin without breakage, we investigated the mechanical performance of microneedle patches composed of 5 × 5 arrays of microneedles (**Table 1**). Smooth force-displacement curves of solid and hollow microneedles (base diameter of 500 μm) (**Figure 2**a), with no evidence of fracture under compression loads of up to 0.40 N per needle (Figure 2b), verify the mechanical strength of the microneedles to puncture the skin without mechanical yielding (Note S1, Supporting Information).[39,40] The resulting deformation of microneedle tips was measured as 35.76 ± 14.50 and 44.50 ± 6.63 μm for solid and hollow microneedles, respectively, indicating similar behavior of both microneedle types under compressive load. Microneedles with a 300 μm base diameter showed weaker mechanical strength, with an average failure force of 0.12 N (Figure S3, Supporting Information), which might be sufficient to penetrate the skin considering the small tip diameter of the microneedles (5 μm). As evidenced by the shear testing data (Figure 2c,d; Figure S4, Supporting Information), although solid microneedles (MN-1) showed superior mechanical performance compared to hollow microneedles (MN-3 and MN-5), the fracture force of the hollow microneedles revealed their acceptable performance to withstand mild shear forces after application. The fracture forces under shear load for MN-3 and MN-5 were 0.79 ± 0.14 and 0.70 ± 0.03 N per needle, respectively. The negligible net displacement at the end of the shear cycle indicates the capability of the 3D-printed hollow microneedles to preserve their structural integrity. The insertion study revealed that less than 0.10 N per needle was required for complete penetration of the microneedles (Figure 2e; Figure S5, Supporting Information). Moreover, the microneedles demonstrated sufficient robustness against multiple skin insertions (Figure 2f). Collectively, the mechanical characterization and skin insertion studies confirmed the robustness of the 3D-printed microneedles against disruptive forces relevant to various dermal applications.

2.3. Surface Modification and Biocompatibility of the Microneedles

Despite the widespread implementation of 3D-printed microneedles for transdermal applications,[6,41,42] the hydrophobic nature of most polymer-based microneedles hinders their usage in many real-life biomedical applications, especially for ISF extraction. Improving the wettability of hollow microneedles could expedite ISF collection and help ensure a continuous fluid flow. Several studies have employed various modification approaches to enhance the hydrophilicity of microneedles and facilitate ISF extraction.[43,44] In this study, the surface of 3D-printed microneedle channels was coated with a silicon oxide layer using chemical vapor deposition (CVD) to increase hydrophilicity, thus enhancing ISF adsorption through the microchannels (**Figure 3**a,b). The presence of hydroxyl groups on the surface of SiO_2 coating plays the key role in its superhydrophilic properties. The wettability of the microneedles was characterized by measuring the static water contact angle (WCA) before and after treatment. The WCA of microneedles decreased from ≈72 to 9° following oxide coating ($p = 0.00001$), indicating a dramatic improvement in hydrophilicity. Additionally, the treated microneedles maintained their improved wettability for 4 weeks (Figure S6, Supporting Information). Figure 3c shows the thickness of the SiO_2 coating on the 3D-printed parts, measured using a stylus profiler. The height difference between bare and coated parts was 1295.84 ± 101.66 nm.

© 2025 The Author(s). Advanced Materials Technologies published by Wiley-VCH GmbH

2365709x, 2025, 22, Downloaded from https://advanced.onlinelibrary.wiley.com/doi/10.1002/admt.202500891 by Koc University, Wiley Online Library on [07/12/2025]. See the Terms and Conditions (https://onlinelibrary.wiley.com/terms-and-conditions) on Wiley Online Library for rules of use; OA articles are governed by the applicable Creative Commons License

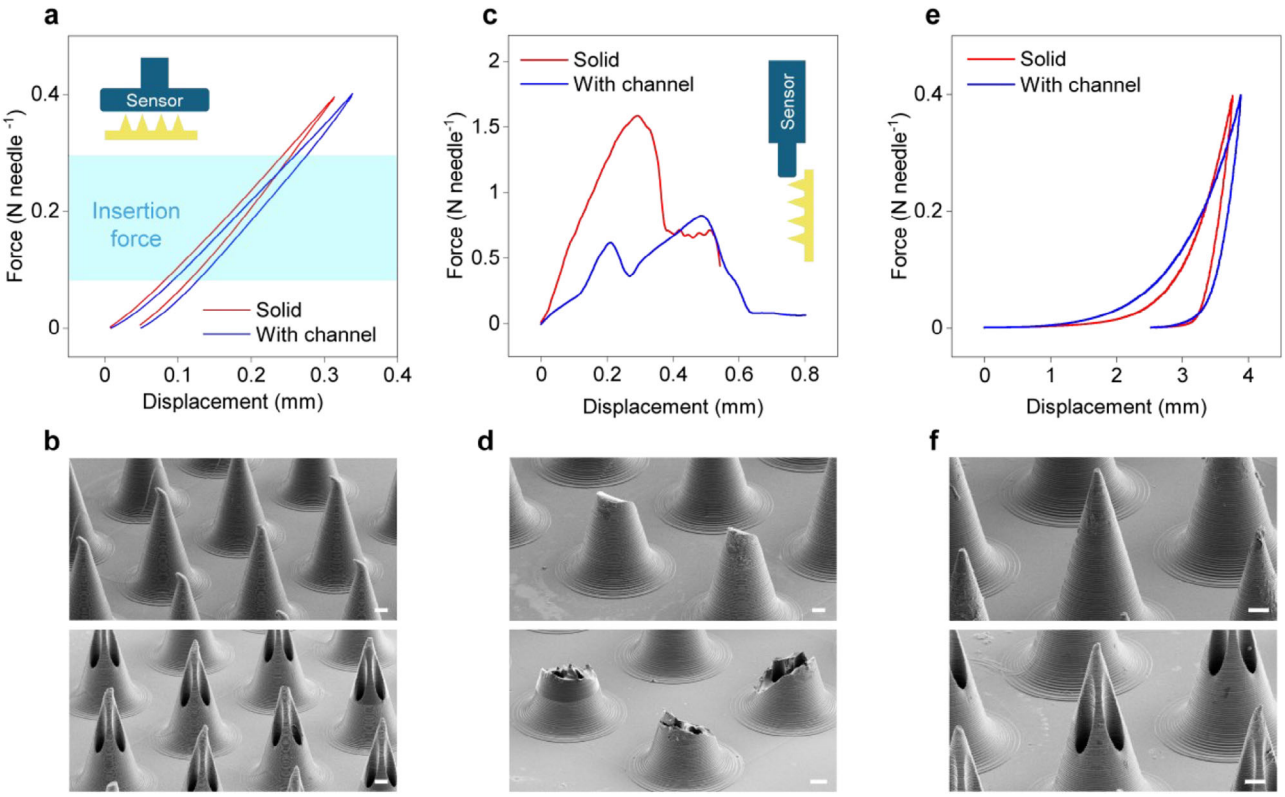


Figure 2. Mechanical characterization of the microneedle patches. a) Mechanical behavior of the microneedle patches under compressive load with a schematic of the experimental setup (inset). b) SEM images of solid and hollow microneedles after the application of compressive force. c) Mechanical performance of the microneedle patches under shear load with a schematic of the test setup (inset). d) SEM images of solid and hollow microneedles after application of shear. e) Mechanical performance of the microneedle arrays when applied to the skin samples. f) SEM images of microneedle arrays after skin penetration experiments. (All mechanical characterization experiments and SEM imaging were performed on microneedles MN-1 and MN-3, the design of which are provided in Table 1). Scale bars are 100 μm.

To evaluate the cytotoxicity of the 3D-printed microneedles before and after SiO_2 coating, NIH/3T3 cells (mouse embryonic fibroblast cell line) were cultured in the presence of microneedles, followed by examination using viability and metabolic activity assays. As shown in Figure 3d and Figure S7a,b (Supporting Information), no notable differences were observed between the live/dead images of the control group and microneedle-immersed groups. Additionally, the cells cultured with microneedles in the medium exhibited comparable cell viability to the control group after 24 and 72 h of immersion in the complete medium, indicating nontoxic effects of the 3D-printed microneedles before and after SiO_2 coating (Figure 3e,f; Figure S7c,d, Supporting Information).

2.4. Liquid Uptake Capability of the Microneedles

The enhancement in water uptake capability of the microneedles was visually observed by inserting them into liquid or agarose gel (**Figure** 4a,b; Figures S8,S9, Supporting Information). To better visualize the liquid flow through microchannels, a microneedle patch with 10 × 10 arrays of microneedles, with a length of 1.5 mm, microchannel diameter of 200 μm, and backing thickness of 2 mm was 3D-printed. Briefly, the microneedles were inserted into a chamber containing blue-dyed artificial ISF (aISF) or agarose gel. To ensure that liquid extraction from the medium was solely attributed to capillary action within the microchannels, the microneedles were carefully positioned to avoid full insertion into the medium. Additionally, a force sensor was integrated into the experimental setup to monitor the interaction force between the microneedles and the agarose gel, thus ensuring consistent conditions across experiments (Figure S8c, Supporting Information). The measured force was ≈0.45 ± 0.04 N.

Upon insertion, the liquid is drawn into the microneedle channels due to capillary action and subsequently collected in the integrated microfluidic module (Note S3, Supporting Information). The SiO_2-coated microneedles exhibited superior performance in fluid collection when inserted into liquid or agarose gel (Figures S10–S12, Supporting Information). While bare microneedles failed to extract any liquid from agarose gel, the SiO_2-coated microchannels were filled with blue-dyed liquid within a few seconds. As demonstrated in Figure 4c, the untreated half of the microneedle patch did not exhibit any water extraction capacity upon insertion into agarose gel, whereas the SiO_2-coated, superhydrophilic microneedles on the same patch initiated liquid extraction immediately upon insertion (Figure S13 and Movie S1, Supporting Information). The treated microchannels turned bluish due to liquid uptake, while no color change was observed

© 2025 The Author(s). Advanced Materials Technologies published by Wiley-VCH GmbH

2365709x, 2025, 22, Downloaded from https://advanced.onlinelibrary.wiley.com/doi/10.1002/admt.202500891 by Koc University, Wiley Online Library on [07/12/2025]. See the Terms and Conditions (https://onlinelibrary.wiley.com/terms-and-conditions) on Wiley Online Library for rules of use; OA articles are governed by the applicable Creative Commons License

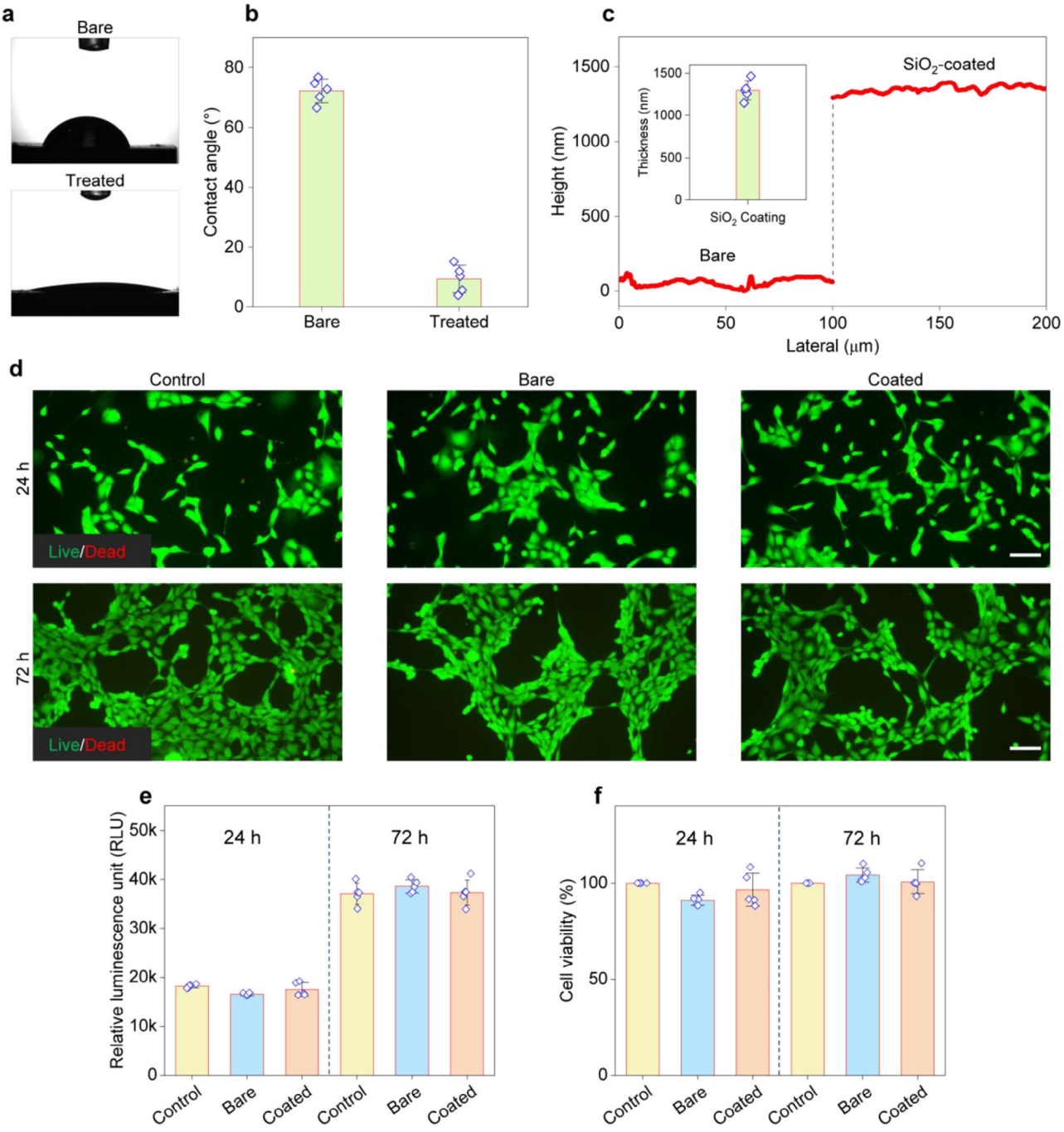


Figure 3. Surface modification of 3D-printed microneedles to enhance the wettability. a) Images of water droplets on surfaces without (top) and with (bottom) hydrophilic coating. b) The measured contact angles of bare and treated samples. c) Surface profile of the 3D-printed sample after SiO_2 coating. Inset: thickness results of the SiO_2-coated samples. d) Representative live (green)/dead (red) images of NIH/3T3 cells after 24 and 72 h of cell culture without (control) and with 3D-printed samples (bare and coated). e) Quantitative analysis of cellular metabolic activity, presented in relative luminescence units (RLU). f) Quantitative analysis of cell viability images. All data are expressed as mean values ± s.d. ($n = 5$). Scale bars are 100 μm.

in the bare microchannels, indicating no liquid uptake. The SiO_2-coated microneedle patch collected 20.07 ± 1.22 and 39.03 ± 1.54 mg of aISF within 1 and 5 min, respectively (Figure 4d). There was only a minor increase (0.82%) in the amount of collected liquid between time points of 5 and 10 min, indicating that the microfluidic chamber was completely filled within ≈5 min. The reduction in the rate of liquid uptake over time could be attributed to the reduced capillary action as the collected liquid fills the microfluidic chamber.

When microneedles were inserted into the liquid aISF, the filling time of the integrated microfluidic module was 57.20 ± 11.40 and 4.03 ± 1.21 s for the bare and treated microneedles,

© 2025 The Author(s). Advanced Materials Technologies published by Wiley-VCH GmbH

2365709x, 2025, 22, Downloaded from https://advanced.onlinelibrary.wiley.com/doi/10.1002/admt.202500891 by Koc University, Wiley Online Library on [07/12/2025]. See the Terms and Conditions (https://onlinelibrary.wiley.com/terms-and-conditions) on Wiley Online Library for rules of use; OA articles are governed by the applicable Creative Commons License

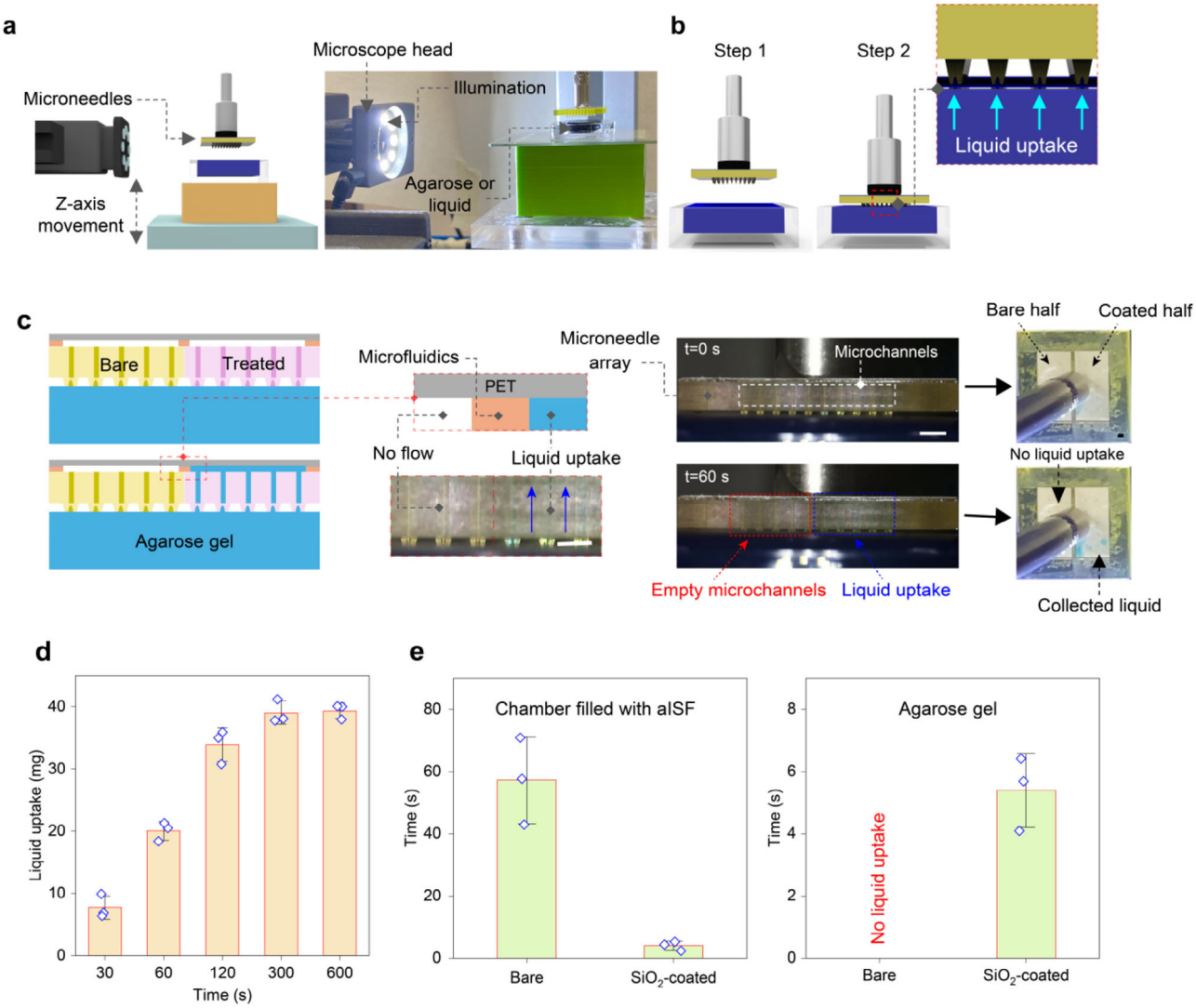


Figure 4. In vitro characterization of the liquid extraction capability of the microneedles. a) Schematic illustration (left) and photographic image (right) of the liquid uptake setup. b) Liquid uptake experiment. c) Schematic (left) and optical images (right) of liquid uptake from agarose gel. d) Liquid uptake of surface modified microneedles from agarose gel over different periods. e) The time required for complete filling of the integrated microfluidic chamber by bare and SiO_2-coated microneedles. Left: liquid collection from aISF chamber and right: liquid collection from agarose gel. All data are expressed as mean values ± S.D. ($n = 3$). Scale bars are 1 mm.

respectively, showing a significant decrease ($p = 0.02$) in the required time to collect a certain amount of aISF using the SiO_2-coated microneedles (Figure 4e, left). This improvement can be attributed to the superhydrophilicity of the microchannels (Note S2, Supporting Information). As mentioned earlier, while bare microneedles could not extract any liquid from agarose gel, SiO_2-coated microneedles filled the microfluidic chamber within 323.90 ± 5.40 s (Figure 4e, right). As expected, the hydrophilic nature of the agarose gel lowers the rate of liquid uptake, thereby increasing the required time to fill the microfluidic chamber. Visual observation of the absorption of blue dye containing liquid in microchannels was somewhat difficult. Therefore, similar experiments were also performed by using a red dye in agarose. As shown in Figure S8d (Supporting Information), dramatic difference is observed in the dye absorption by SiO_2 treated and untreated microneedles with single or double microchannels per needle after 5 minutes of insertion into agarose.

2.5. In Vitro and Ex vivo Parametric Study on Liquid Uptake

First, we studied the effect of different parameters on ISF collection from agarose hydrogel. The experimental setup for in vitro experiments comprised a transparent chamber containing blue-stained agarose hydrogel, a microneedle patch, and a vacuum source (**Figure** 5a). To explore the effect of applied vacuum on the liquid collection, the vacuum pressure was varied between −2 and −20 kPa. As discussed earlier, bare microneedles were unable to collect any liquid from agarose hydrogel by capillary force. Vacuum pressures down to −5 kPa was insufficient to initiate the

© 2025 The Author(s). Advanced Materials Technologies published by Wiley-VCH GmbH

2365709x, 2025, 22, Downloaded from https://advanced.onlinelibrary.wiley.com/doi/10.1002/admt.202500891 by Koc University, Wiley Online Library on [07/12/2025]. See the Terms and Conditions (https://onlinelibrary.wiley.com/terms-and-conditions) on Wiley Online Library for rules of use; OA articles are governed by the applicable Creative Commons License

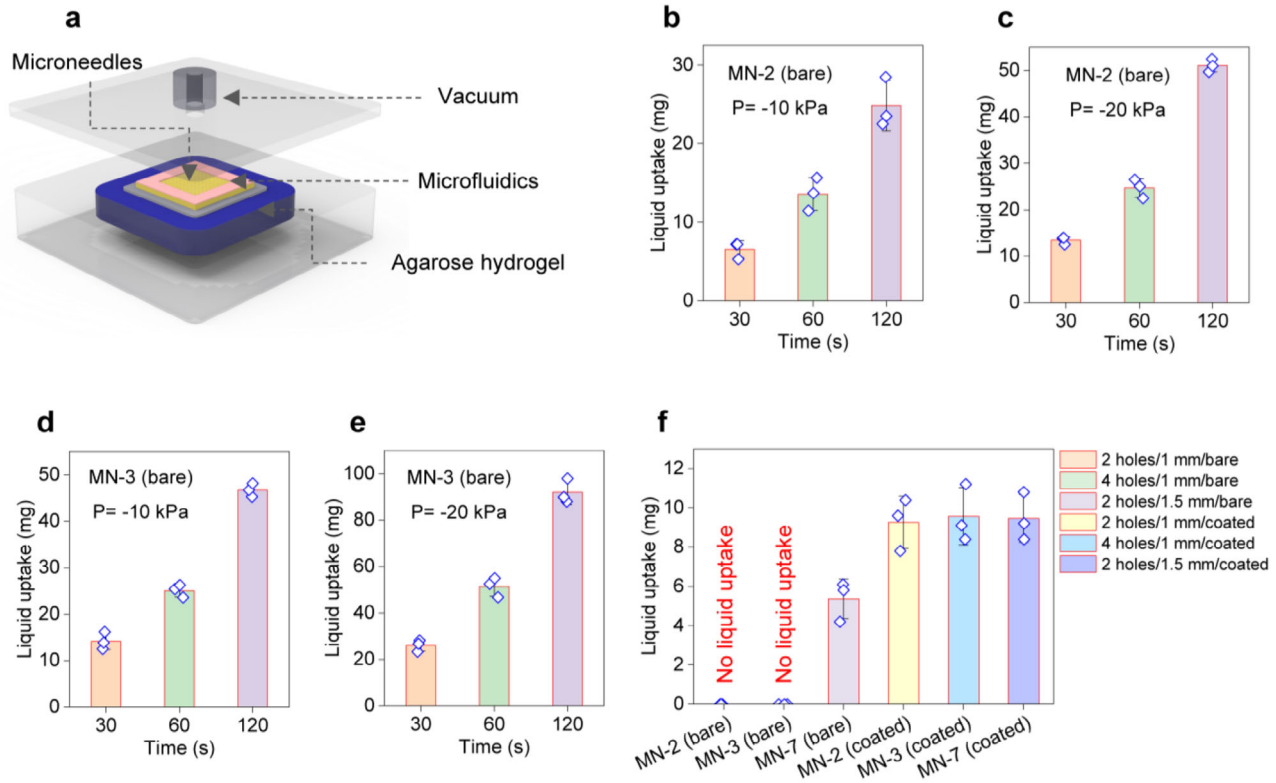


Figure 5. Effect of different parameters on the extraction capacity of the microneedles. a) Schematic illustration of the setup utilized for the liquid uptake experiments from agarose hydrogel. Liquid uptake by bare microneedles with two microchannels using vacuum pressure of b) −10 kPa and c) −20 kPa. Liquid uptake by bare microneedles with four microchannels using vacuum pressure of d) −10 kPa and e) −20 kPa. f) Liquid uptake from rat skin samples under a vacuum pressure of −40 kPa after 30 min.

liquid flow through the microchannels. However, increasing the vacuum level to below −10 kPa enabled the microneedles to extract liquid from agarose gel. For a vacuum pressure of −10 kPa, the collected liquid increased from 6.56 ± 0.89 to 24.85 ± 2.62 mg when the extraction time increased from 30 to 120 s (Figure 5b). Upon application of a vacuum pressure of −20 kPa, the collected liquid almost doubled (Figure 5c). While 13.60 ± 1.71 mg of liquid was collected after 60 s for −10 kPa, the corresponding value was 24.70 ± 1.66 mg at −20 kPa, representing an 81.6% increase in liquid extraction due to the reduced vacuum pressure. Given the laminar flow inside the needle microchannels, these results are in good agreement with the classical Hagen-Poiseuille model (Note S4, Supporting Information).

To investigate the effect of the number of microchannels on liquid extraction, microneedles were fabricated with designs of 2 and 4 microchannels per needle (MN-2 and MN-3). As illustrated in Figure 5d, for a vacuum pressure of −10 kPa and an extraction time of 120 s, the liquid uptake increased from 24.85 ± 2.62 to 46.77 ± 1.18 mg when the number of microchannels increased from 2 to 4, indicating nearly doubled liquid collection in microneedles with 4 microchannels per needle. Similar behavior was observed at a vacuum pressure of −20 kPa (Figure 5e). Since the microchannels in each needle are connected in a parallel manner, assuming identical channels with the same frictional loss, the liquid uptake rate is linearly correlated with the number of channels (Note S5, Supporting Information).

Next, the effect of SiO_2 coating on enhancing the liquid uptake from rat skin samples was examined (Figure S14, Supporting Information). As evidenced in Figure 5f, bare microneedles with a length of 1 mm could not extract any ISF after 30 min under an average vacuum pressure of ≈−40 kPa. This might stem from incomplete penetration of the microneedles into the skin, leaving part of the microchannels exposed to air rather than being inside the tissue, as revealed by the formation of suction blisters on the skin samples (Figure S15, Supporting Information). Moreover, the presence of ISF inside and around the skin pores after microneedle removal indicates that the ISF in the dermis was unable to overcome the resistance forces against liquid flow. Increasing the needle length to 1.5 mm resulted in an ISF extraction rate of 0.18 ± 0.03 mg min^{-1} per microneedle patch (Figure 5f). SiO_2-coated microneedles showed superior extraction capacity from skin samples. Microneedles with 2 and 4 channels were able to extract 0.31 ± 0.03 and 0.32 ± 0.04 mg min^{-1} per microneedle patch ($p = 0.007$ and $p = 0.008$, respectively), confirming the effectivity of the superhydrophilic coating on enhancing the ISF extraction. These results suggest that increasing the number of microchannels per needle from 2 to 4 did not have a considerable effect on the amount of extracted ISF from skin samples. As shown in Figure 5f, although SiO_2 coating increased the ISF extraction rate for microneedles with 1.5 mm length from 0.18 ± 0.03 to 0.32 ± 0.03 mg min^{-1} per microneedle patch, the extraction rate of SiO_2-coated microneedles with lengths of 1 and 1.5 mm were almost the same.

© 2025 The Author(s). Advanced Materials Technologies published by Wiley-VCH GmbH

2365709x, 2025, 22, Downloaded from https://advanced.onlinelibrary.wiley.com/doi/10.1002/admt.202500891 by Koc University, Wiley Online Library on [07/12/2025]. See the Terms and Conditions (https://onlinelibrary.wiley.com/terms-and-conditions) on Wiley Online Library for rules of use; OA articles are governed by the applicable Creative Commons License

2.6. Quantitative Colorimetric Analysis and Detection Of Biomarkers

As previously illustrated, the developed microneedle patches offer great promise for minimally invasive and effective ISF extraction, enabling colorimetric analysis of various biomarkers present in ISF. For proof-of-concept demonstration, urea and pH were selected as the target biomarkers. Both of these biomarkers could provide crucial information associated with health problems such as kidney and renal malfunctions. For healthy individuals, the normal urea level ranges from 3 to 7.5 mM, whereas for patients with chronic kidney dysfunctions, the urea level might increase up to 8–15.1 mM.[45,46] While the normal blood pH level is maintained between 7.35 and 7.45 by pH buffering substances like proteins and phosphates,[47] due to the lack of buffering capacity in ISF, the pH of ISF can deviate from the normal range (6.6–7.6).[47,48] For instance, the pH level ranges from 5.45 to 8.65 in chronic wounds, and it may decrease to 5.4 in inflamed tissues.[49,50]

Most of the previously reported methods for measuring urea rely on electrochemical sensors,[51,52] NMR,[53] or HPLC.[54] The colorimetric method implemented here for the detection of urea is based on the pH rise resulting from the urease-catalyzed hydrolysis of urea, thereby releasing ammonium and hydroxide ions into the solution (Equation 1)[55]

$$NH_2(CO)NH_2 + 3H_2O \xrightarrow{\text{Urease}} 2NH_4^+ + HCO_3^- + OH^- \quad (1)$$

By immobilizing urease onto colorimetric pH papers, the hydrolysis reaction of urea is effectively catalyzed, thus altering the pH level and color of the pH paper. The resulting changes in the color intensity of the pH papers are well-correlated to the urea concentration. The detection range for urea was selected between 1 and 20 mM, relevant to physiological urea concentrations in ISF under normal or disease states. As shown in **Figure 6a**, the color of sensing regions changed from dark green to dark blue when the urea concentration increased from 1 to 20 mM. Quantitative analysis of RGB values in the captured images showed a decrease in intensities at the R and G channels and an increase in B channel with increasing urea concentrations. Since the B channel intensity values exhibited the most significant changes with urea concentration, the B channel was selected for quantification. During the detection of pH, the color changed from brown green to dark blue, as the pH increased from 6.45 to 8.20, relevant to the physiological pH level in ISF (Figure 6b).

The corresponding calibration curve for urea detection showed a linear behavior with the correlation coefficient of $R^2 = 0.98$ and limit of detection (LOD = $3.3\sigma/S$, where σ is the standard deviation and S is the slope of calibration curve) of 0.83 mM (Figure 6c). Quantitative analysis of the captured images showed a linear decrease (correlation coefficient of 0.98) in R channel intensity values with increasing pH (Figure 6d). Although the rate of urea hydrolysis into ammonium and hydroxide can be affected by the solution pH,[56] thus influencing the required incubation period, the final RGB intensities across different urea concentrations were not affected considerably by the solution pH (Figure 6e). We further characterized the performance of the colorimetric urea assay against the presence of possible interferents in ISF. As evidenced by the results presented in Figure 6f, the color of urea assay was negligibly influenced upon addition of target interferents.

Next, the colorimetric assays were integrated with the 3D-printed microneedles to validate the performance of the developed technique for biomarker detection in the extracted ISF. Agarose hydrogel was selected as the skin model to mimic the penetration of microneedles into the skin. Due to the improved water extraction capacity of the SiO_2-coated microneedles owing to their superhydrophilicity, they were inserted into the agarose hydrogel without applying vacuum. As shown in Figure 6g,h, there was a good agreement between the detected urea and pH levels and the actual values. Finally, the microneedle patch with the colorimetric assays was inserted into equilibrated skin samples to detect the urea and pH level. Once the extracted ISF came into contact with the colorimetric assays, the color change showed the urea and pH levels (Figure 6I; Movie S2, Supporting Information). Overall, the colorimetric results revealed the great potential of integrating colorimetric assays into superhydrophilic microneedles with passive ISF extraction capability for urea and pH sensing.

3. Conclusion

In this study, we developed a 3D-printed microneedle patch with superhydrophilic microchannels to effectively and continuously extract dermal ISF for health monitoring applications. Conical hollow microneedles with different lengths, base diameters, and microchannel counts were printed via high-precision PμSL technology using a biocompatible resin. Mechanical testing experiments revealed the excellent mechanical resistance of the microneedles against disruptive forces. Cytotoxicity experiments validated the biocompatibility of the 3D-printed microneedle patches before and after silicon oxide layer deposition. To enhance hydrophilicity, we deposited a thin SiO_2 layer on the microneedle patch and decreased its static water contact angle from ≈72 to 9°. The superhydrophilic coating imparted microneedles with liquid uptake capability from agarose hydrogel. Although increasing the number of microchannels per needle from 2 to 4 greatly enhanced the extraction capability of the microneedles in vitro, there was negligible effect on the extraction rate from the rat skin samples. Hydrophilic microneedles with a height of 1 mm showed superior ISF extraction capability from rat skin samples compared to the bare microneedles. However, increasing the height of SiO_2-coated microneedles from 1 to 1.5 mm did not result in an increase in ISF extraction from the skin samples. The SiO_2-coated MNs extracted ≈0.3 mg min^{-1} per patch, confirming its effectiveness for ISF sampling-based health monitoring devices. We successfully demonstrated the applicability of the platform for detecting ISF biomarkers by integrating a microfluidic module and colorimetric assays for urea and pH. Upon ISF extraction from rat skin samples, the urea and pH levels in the ISF were measured by recording the RGB values of the colorimetric assays. This superhydrophilic microneedle patch could be integrated into various ISF-based devices to expand their application for detecting a wide spectrum of biomarkers in ISF and holds a significant promise to benefit health monitoring and disease management.

© 2025 The Author(s). Advanced Materials Technologies published by Wiley-VCH GmbH

2365709x, 2025, 22, Downloaded from https://advanced.onlinelibrary.wiley.com/doi/10.1002/admt.202500891 by Koc University, Wiley Online Library on [07/12/2025]. See the Terms and Conditions (https://onlinelibrary.wiley.com/terms-and-conditions) on Wiley Online Library for rules of use; OA articles are governed by the applicable Creative Commons License

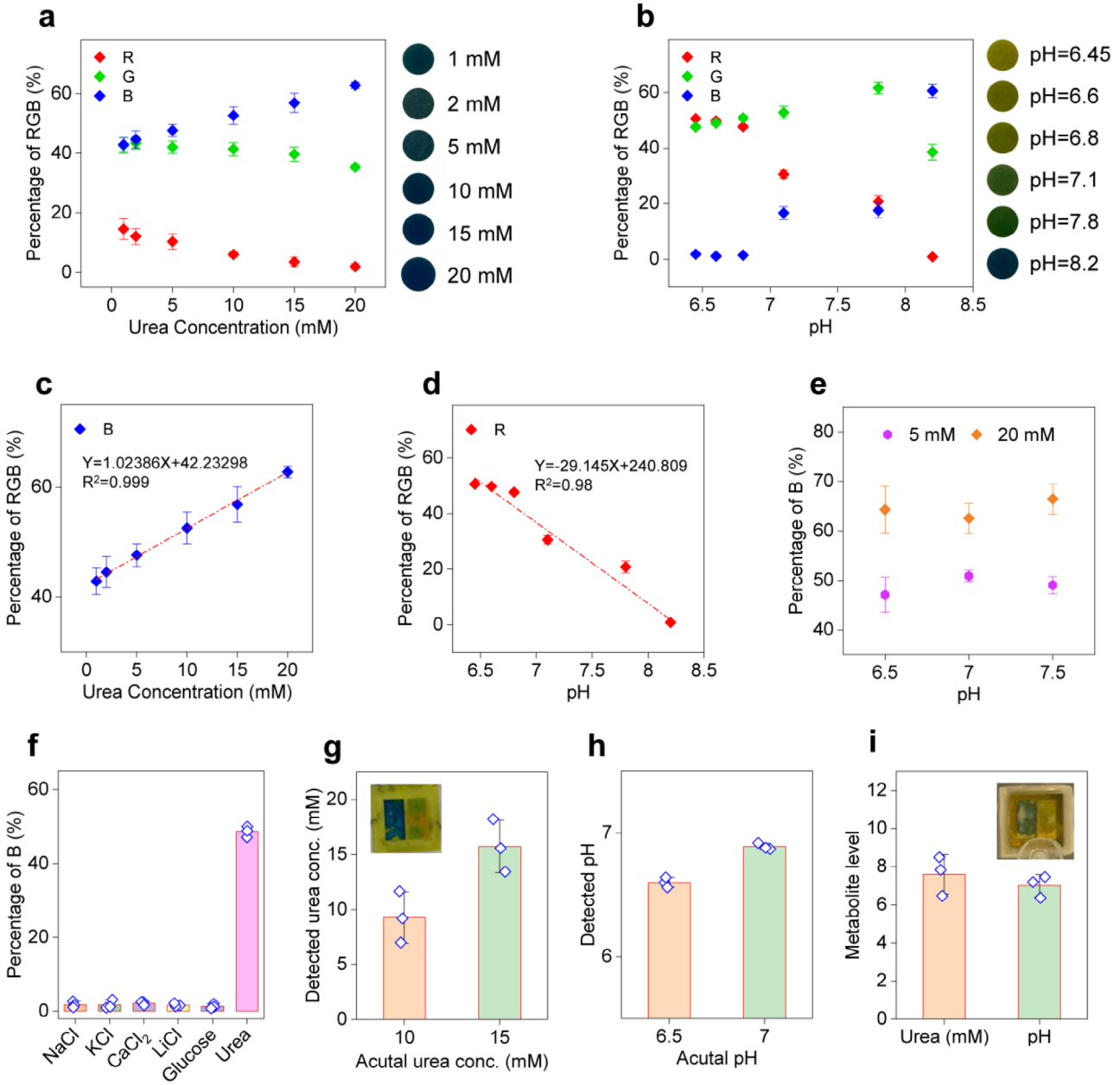


Figure 6. Colorimetric detection of urea and pH. Colors and RGB intensities during the detection of a) urea and b) pH. c) The linear correlation between the intensity of B and urea concentration. d) The linear correlation between the intensity of R and pH level. e) Effect of pH on the urea detection. f) Response of the urea assay against various interferents. g) In vitro urea detection on agarose gel with pH of 7. h) In vitro pH detection on agarose gel with urea concentration of 10 mM. i) Ex vivo response of the urea and pH assays and urea on rat skin. All data are expressed as mean values ± S.D. ($n = 3$).

4. Experimental Section

Materials: PDMS (Sylgard 184 Silicone Elastomer) was obtained from Dow Corning (MI, USA). Biocompatible resin (BIO) was purchased from Boston Micro Fabrication (BMF Material Technology Inc., Shenzhen, China). Urease (from Canavalia ensiformis, Jack bean, type III), agarose (for molecular biology), sodium chloride (NaCl), potassium chloride (KCl), calcium chloride ($CaCl_2$), and lithium chloride (LiCl) were bought from Sigma-Aldrich (MO, USA). D(+)-Glucose and urea crystalline pure were obtained from neoFroxx. Double-sided tape (9495 LE 300 LSE) was obtained from 3 M (MN, USA). Transparent polyethylene terephthalate (PET) films were purchased from MG Chemicals (Burlington, Canada). Universal pH indicator was obtained from Macherey Nagel (Duren, Germany).

Design of Microneedle Arrays and 3D Printing: The microneedle patches were fabricated from a biocompatible resin using PμSL. The designs were prepared using SolidWorks 3D design software (Figure S16, Supporting Information), and then imported into VoxelDance software to be sliced into 2D images (Figure S17, Supporting Information), which served as the UV masks. The microneedles were printed using a microArch S230 (Boston Micro Fabrication) 3D printer. The stage and needle parts of microneedle patches were printed in 20 and 5 μm thick layers, respectively. Despite

© 2025 The Author(s). Advanced Materials Technologies published by Wiley-VCH GmbH

2365709x, 2025, 22, Downloaded from https://advanced.onlinelibrary.wiley.com/doi/10.1002/admt.202500891 by Koc University, Wiley Online Library on [07/12/2025]. See the Terms and Conditions (https://onlinelibrary.wiley.com/terms-and-conditions) on Wiley Online Library for rules of use; OA articles are governed by the applicable Creative Commons License

the higher print time, 5 µm thick layers ensured maximum accuracy and minimum needle tip size (Figure 1c; Figures S1 and S2, Supporting Information). After importing the 2D gray images into the microArch S230, the 3D printer vat was filled with BIO resin, followed by UV exposure (405 nm light wavelength) to only the white zones of the 2D images. Figure S17 (Supporting Information) shows the representative UV masks at different stages of the 3D printing process. Once the 3D printing was completed, the microneedle patches were scraped off from the stage and washed using 99% isopropyl alcohol. Then, FormCure (Formlabs) was used to post-cure the microneedles under 405 nm radiation for 2 h at 50 °C.

All microneedle patches were printed in 10 × 10 arrays except for the mechanical characterization experiments, where 5 × 5 arrays were used to perform the tests. Each patch contained conical microneedles of 1 mm in height and center-to-center distance, base diameter of 300 and 500 µm, and microchannel diameter of 50 and 100 µm (Table 1).

Mechanical Characterization of 3D-Printed Microneedle Arrays: The mechanical properties of the 3D-printed microneedle patches were measured using a force-displacement test setup comprising a force gauge (MARK-10) and a Z-axis stage (Figures S3–S5, Supporting Information). The mechanical behavior of solid and hollow microneedles with different diameters was examined under compression load and shear load, followed by performing the skin penetration tests. Briefly, to study the mechanical stability of microneedles under compression load, the microneedle patch was placed on the Z-axis stage platform with needles facing toward the force sensor. The measurement started once the microneedle tips touched the force sensor and continued until a maximum force of 0.4 N per needle was obtained (Figure S3, Supporting Information).

To examine the mechanical behavior of microneedle patches under shear load, the microneedle patch was attached to a rigid platform, ensuring the microneedles were oriented horizontally. The sensor tip was replaced with another tip to be able to apply the force to a single microneedle (Figure S4, Supporting Information). For each microneedle, the measurement was continued until the fracture point was achieved. To assess the skin insertion ability, the microneedles were applied to fresh rat skins while the needle tips were facing toward the skin (Figure S5, Supporting Information). The application of vertical force on microneedle patches was continued until a predefined force of 0.4 N per needle was achieved. All mechanical characterization experiments were performed on microneedle patches with 5 × 5 arrays and a patch area of 7 × 7 mm^2.

Following each experiment, SEM and optical microscopy images of microneedles were obtained to examine the robustness of the 3D-printed microneedles against mechanical deformations.

Morphological Characterization of Microneedles: The microneedle morphologies were characterized using optical and scanning electron microscopy. Optical images were captured using a motorized microscope (MRCL700 3D imager pro, Microqubic AG, Switzerland). SEM imaging was performed using ZEISS (Zeiss, Ultra Plus, Germany) scanning electron microscope operated at 10 kV. Before SEM imaging, the sample surfaces were coated with a 50 nm-thick gold layer. Additionally, SEM images were used to examine the robustness of hollow microneedles after performing the mechanical characterization experiments. Furthermore, top view SEM images of the microneedles were processed using MATLAB (MathWorks, MA, USA) to obtain the diameter of microchannels in the fabricated hollow microneedles (Figures S1,S2, Supporting Information).

Hydrophilic Coating and Characterization: To increase the hydrophilicity, the 3D-printed microneedles were coated with a thin layer of SiO_2 using CVD. SENTECH ICP-CVD SI-500 was utilized to deposit an oxide layer of ≈1200 nm thickness (Figure 3c). To mitigate any adverse effect of the elevated temperature inside the CVD chamber on the 3D-printed samples, the deposition process was segmented into four stages, each with a 300 nm thickness. The thickness of the oxide layer was measured using a stylus surface profilometer (Dektak, Bruker). An optical tensiometer (ThetaLite TL 101, Biolin) was employed to measure the static water contact angle of the surfaces by placing 2 µL of DI water on the untreated and SiO_2-coated 3D-printed sample films at room temperature. The samples were printed with the surface area of 2 × 2 cm^2, and the water droplets were placed on different parts of the samples. Contact angles were reported as the mean value of measured water contact angles on five different locations on the surface under the same conditions.

Integration of Microfluidic Module: A microfluidic layer was integrated into the microneedle patch to provide a collection chamber for the extracted liquid. The chamber designs were prepared using AutoCAD (Autodesk, USA) and then transferred onto a double-sided tape (9495 LE 300 LSE) using a UV laser-cutting machine (ProtoLaser U4, LPKF, Germany). The as-prepared microfluidic layer was attached to the backside of the microneedle patches to serve as the ISF collection chamber, followed by enclosing the chamber using a PET layer.

In Vitro ISF Extraction Experiments: The liquid collection capability of the 3D-printed microneedles was evaluated by inserting the microneedle tips into aISF and 1.4 wt.% agarose gel. The aISF solution was prepared according to the procedure previously reported in the literature.[57] The microneedle patch was affixed on a force sensor tip, while the chamber containing the blue-dyed agarose gel or aISF was placed on a Z-axis stage to enable vertical movement between the microneedle tips and the chamber. The force sensor enabled the detection of initial contact between the microneedle tips and the liquid or agarose gel. A microscope equipped with a camera (MRCL700 3D imager pro, Microqubic) was integrated into the experimental setup for real-time video recording of liquid extraction (Figure S8, Supporting Information). Once the initial contact was detected using the force sensor, the microneedles were inserted into the liquid medium by moving the Z-axis stage while ensuring a portion of their length remained outside the medium (Figures S9–S11, Supporting Information). A smartphone camera (iPhone 11, Apple, USA) captured the videos of the microfluidic chamber filling (Figure S12, Supporting Information).

The vacuum was generated using A PDMS-based finger-actuated system, which was developed in the previous study.[25] To be able to measure the vacuum level, the pressure in the system was monitored using a pressure sensor (BMP 280, Bosch). The pressure data was recorded using an Arduino board, which enabled the transfer of acquired pressure data to a personal computer. To investigate the effect of vacuum level on ISF extraction, vacuum pressures of −2 to −20 kPa was tested during in vitro experiments.

ISF Collection From Rat Skin Ex Vivo: Rat skin samples were collected in from Wistar rats (in compliance with the guidelines and usage specifications of Koç University Animal Research Facility of Center for Translational Medicine, 2024.HADYEK.017) immediately after euthanasia and kept at −80 °C until use. The skin samples were collected from dorsal side of the rats, which was entirely shaved before excision. Square samples (area of 2 × 2 cm^2) were thawed and placed in a transparent chamber with a PDMS layer underneath the skin samples (Figure S14, Supporting Information). Before inserting the microneedles, the skin samples were entirely dried using a paper towel to remove any remaining water residues on the skin surface. For better visualization of ISF extraction, blue-stained filter papers were embedded in the microfluidic chamber. After placing the skin samples in the transparent chamber, the microneedle patch was administered. Double-sided tapes provided secure attachment of the microneedles to the skin, while ensuring reliable sealing to help minimize vacuum drop during the experiments. The experiments were performed at an average vacuum pressure of ≈−40 kPa. Microneedle patches were weighted using a high precision laboratory scale before and after each experiment to determine the amount of extracted ISF.

Forming the Colorimetric Assay: To prepare the sensing assay for urea, a similar approach to the previous studies was adopted here.[58] In brief, a urease solution with a concentration of 10 mg mL^{-1} was prepared in deionized water. To perform the experiments of obtaining the calibration curve, small pieces of pH paper were cut using a laser in circular shapes with a diameter of 3 mm. Additionally, rectangular shapes of pH papers (5.5 × 12 mm^2) were laser-cut to be integrated to the microfluidic module. To yield the urea assay, 2 and 20 µL of the urease solution were immobilized onto the circular and rectangular pH papers, respectively, followed by drying under vacuum for 15 min. For pH sensing, the circular and rectangular pH papers were utilized without any modification.

Color Development and Biomarker Detection of the Colorimetric Assay: Standard solutions of aISF with urea concentration ranging from 1–20 mM and pH values ranging from 6.4–8.2 were prepared. The pH of standard

© 2025 The Author(s). Advanced Materials Technologies published by Wiley-VCH GmbH

2365709x, 2025, 22, Downloaded from https://advanced.onlinelibrary.wiley.com/doi/10.1002/admt.202500891 by Koc University, Wiley Online Library on [07/12/2025]. See the Terms and Conditions (https://onlinelibrary.wiley.com/terms-and-conditions) on Wiley Online Library for rules of use; OA articles are governed by the applicable Creative Commons License

solutions was adjusted using 0.1 M HCl and 0.1 M NaOH solutions. A commercial pH meter (Orion Dual Star, Thermo Scientific, MA, USA) was utilized to measure the pH level. To extract the reference markers for obtaining the calibration curves, 2 µL of the standard solutions were dropped onto the circular papers, followed by incubation at 37 °C for 15 min. It should be noted that for the pH assay, no incubation period was required, as the color change was visible after a few seconds. A smartphone rear camera (iPhone 11, Apple, CA, USA) was used to capture the images under controlled lighting conditions using its regular camera application. To increase the reliability of the implemented colorimetric analysis, room light was used for image acquisition, and the distance and orientation between the samples and the smartphone were kept the same to minimize the effect of external interferences. All images were captured using the same smartphone camera. Then, the images were analyzed using ImageJ software to extract the color intensity values at R, G, and B channels. A layer containing color reference markers was printed using a color laser printer with colors that matched the colors determined after performing calibration experiments. The selectivity of the urea assay was characterized by adding NaCl, $CaCl_2$, KCl, LiCl, and glucose solutions with concentrations of 5 mM to the urea assays.

For in vitro urea and pH sensing, 1.4 wt.% agarose gels with urea concentrations of 10 and 15 mM and pH values of 6.5 and 7.0 were prepared. The as-prepared rectangular colorimetric assays were integrated into the microneedles, and inserted into the agarose gel for liquid uptake. After extraction and incubation, the colorimetric responses of the assays were recorded using the smartphone camera for further analysis. For ex vivo experiments, skin samples were immersed in aISF solutions with urea and pH levels of 10 mM and 6.5, respectively, for 24 h to reach an equilibrated state. Before microneedle application, the skin samples were carefully dried using paper towels, followed by an air gun to ensure complete removal of the remaining surface moisture. The PDMS-based vacuum source was employed as the vacuum source for ISF extraction.

Cell Culture and Cell Viability Assay: To investigate the biocompatibility of the employed microneedles, in vitro cell viability experiments were performed using mouse embryonic fibroblast NIH/3T3 cell line. The complete medium was made of Dulbecco's Modified Eagle's Medium (DMEM, Biowest) supplemented with 10% Fetal Bovine Serum (FBS, Biowest) and 1% penicillin/streptomycin (PS, Gibco). The cells were cultured in a 24-well cell culture plate at a density of 1.5×10^4 cells per well with a complete medium. After allowing overnight attachment of the cells, microneedles were entirely immersed into the complete medium, and cells were treated for 3 days. The seeded cells were stained with Calcein AM (Invitrogen) and propidium iodide (PI, Sigma) to assess the live/dead cells at 24 and 72 h after treatment. Briefly, Calcein AM (1 µM) and PI (5 µg mL^{-1}) dye solutions were prepared in a complete medium, and cells were incubated for 30 min at 5% CO_2 and 37 °C. At the end of the incubation, wells were washed twice with the complete medium, and the required volume of fresh complete medium was left in the wells before imaging. Live/dead cells were monitored using a fluorescence microscope. Metabolic activity was measured with CellTiter-Glo (Promega) luminescent cell viability assay according to manufacturer's instructions at 24 and 72 h after treatment. Luminescence signal for untreated control cells and microneedle treated cells were recorded with a microplate reader (BioTek, Agilent).

Statistical Analysis: All results were presented as mean ± SD (standard deviation). P-values were calculated using an unpaired t-test with a two-tailed distribution.

Supporting Information

Supporting Information is available from the Wiley Online Library or from the author.

Acknowledgements

T.A. and L.B. are supported by The Scientific and Technological Research Council of Turkey (TUBITAK) through 2232 (#118C295) and 3501 (120M363) programs. L.B. acknowledges European Research Council (ERC) (Grant No. 101043119). Authors gratefully acknowledge Koç University Nanofabrication and Nano-characterization Center (N2Star) and Koç University Research Center for Translational Medicine (KUTTAM) for infrastructure access.

Conflict of Interest

Patent application regarding the proposed method is in progress.

Data Availability Statement

The data that support the findings of this study are available from the corresponding author upon reasonable request.

Keywords

3D printing, colorimetric sensing, hollow microneedles, hydrophilic, interstitial fluid, ISF sampling

Received: May 2, 2025
Revised: July 2, 2025
Published online: August 4, 2025

[1] Y. Yang, W. Gao, *Chem. Soc. Rev.* **2019**, *48*, 1465.
[2] J. Min, J. Tu, C. Xu, H. Lukas, S. Shin, Y. Yang, S. A. Solomon, D. Mukasa, W. Gao, *Chem. Rev.* **2023**, *123*, 5049.
[3] M. Friedel, I. A. P. Thompson, G. Kasting, R. Polsky, D. Cunningham, H. T. Soh, J. Heikenfeld, *Nat. Biomed. Eng.* **2023**, 1541.
[4] M. Bariya, H. Y. Y. Nyein, A. Javey, *Nat. Electron.* **2018**, *1*, 160.
[5] P. P. Samant, M. M. Niedzwiecki, N. Raviele, V. Tran, J. Mena-Lapaix, D. I. Walker, E. I. Felner, D. P. Jones, G. W. Miller, M. R. Prausnitz, *Sci. Transl. Med.* **2020**, *12*, aaw0285.
[6] H. Teymourian, F. Tehrani, K. Mahato, J. Wang, *Adv. Healthcare Mater.* **2021**, *10*, 2002255.
[7] R. Ibrahim, J. M. Nitsche, G. B. Kasting, *J. Pharm. Sci.* **2012**, *101*, 2094.
[8] H. Haslene-Hox, E. Oveland, K. C. Berg, O. Kolmannskog, K. Woie, H. B. Salvesen, O. Tenstad, H. Wiig, *PLoS One* **2011**, *6*, 19217.
[9] U. Kiistala, *J. Invest. Dermatol.* **1968**, *50*, 129.
[10] S. Schmidt, R. Banks, V. Kumar, K. H. Rand, H. Derendorf, *J. Clin. Pharmacol.* **2008**, *48*, 351.
[11] Á. Cárcamo-Martínez, B. Mallon, J. Domínguez-Robles, L. K. Vora, Q. K. Anjani, R. F. Donnelly, *Int. J. Pharm.* **2021**, *599*, 120455.
[12] M. Zheng, T. Sheng, J. Yu, Z. Gu, C. Xu, *Nat. Rev. Bioeng.* **2023**, *2*, 324.
[13] M.-N. Chien, Y.-J. Chen, C.-H. Bai, J.-T. Huang, *Micromachines* **2022**, *13*, 478.
[14] Y. Dong, S. Mao, S. Chen, J. Ma, N. Jaffrezic-Renault, Z. Guo, *TrAC Trends Anal. Chem.* **2024**, *180*, 117891.
[15] J. Li, M. Wei, B. Gao, *ACS Sens.* **2024**, *9*, 1149.
[16] C. Wu, Q. Yu, C. Huang, F. Li, L. Zhang, D. Zhu, *Acta Pharm. Sin. B* **2024**, *14*, 5161.
[17] X. He, J. Sun, J. Zhuang, H. Xu, Y. Liu, D. Wu, *Dose-response* **2019**, *17*.
[18] L. K. Vora, A. H. Sabri, P. E. McKenna, A. Himawan, A. R. J. Hutton, U. Detamornrat, A. J. Paredes, E. Larrañeta, R. F. Donnelly, *Nat. Rev. Bioeng.* **2023**, *2*, 64.
[19] I. Rahmi Ausri, S. Sadeghzadeh, S. Biswas, H. Zheng, P. GhavamiNejad, M. Dieu Thao Huynh, F. Keyvani, E. Shirzadi, F. A. Rahman, J. Quadrilatero, A. GhavamiNejad, M. Poudineh, I. R. Ausri, S. Sadeghzadeh, S. Biswas, H. Zheng, P. GhavamiNejad, M. D. T. Huynh, F. Keyvani, E. Shirzadi, M. Poudineh, F. A. Rahman, J. Quadrilatero, A. GhavamiNejad, *Adv. Mater.* **2024**, *36*, 2402009.

© 2025 The Author(s). Advanced Materials Technologies published by Wiley-VCH GmbH

2365709x, 2025, 22, Downloaded from https://advanced.onlinelibrary.wiley.com/doi/10.1002/admt.202500891 by Koc University, Wiley Online Library on [07/12/2025]. See the Terms and Conditions (https://onlinelibrary.wiley.com/terms-and-conditions) on Wiley Online Library for rules of use; OA articles are governed by the applicable Creative Commons License

[20] Y. Li, Y. Wang, R. Mei, B. Lv, X. Zhao, L. Bi, H. Xu, L. Chen, *ACS Sens.* **2024**, *9*, 2567.
[21] Y. Dai, J. Nolan, E. Madsen, M. Fratus, J. Lee, J. Zhang, J. Lim, S. Hong, M. A. Alam, J. C. Linnes, H. Lee, C. H. Lee, *ACS Appl. Mater. Interfaces* **2023**, *15*, 56760.
[22] X. Li, X. Huang, J. Mo, H. Wang, Q. Huang, C. Yang, T. Zhang, H. Chen, T. Hang, F. Liu, *Adv. Sci.* **2021**, *8*, 2100827.
[23] Y. Pang, Y. Li, K. Chen, M. Wu, J. Zhang, Y. Sun, Y. Xu, X. Wang, Q. Wang, X. Ning, D. Kong, *Small* **2024**, *20*, 2305838.
[24] S. Kusama, K. Sato, Y. Matsui, N. Kimura, H. Abe, S. Yoshida, M. Nishizawa, *Nat. Commun.* **2021**, *12*, 658.
[25] T. Abbasiasl, F. Mirlou, H. Mirzajani, M. J. Bathaei, E. Istif, N. Shomalizadeh, R. E. Cebecioğlu, E. E. Özkahraman, U. C. Yener, L. A. Beker, *Adv. Mater.* **2024**, *36*, 2304704.
[26] Y. Xie, J. He, W. He, T. Iftikhar, C. Zhang, L. Su, X. Zhang, *Adv. Sci.* **2024**, *11*, 2308716.
[27] J. Cheng, J. Huang, Q. Xiang, H. Dong, *Anal. Chim. Acta* **2023**, *1255*, 341101.
[28] M. Parrilla, U. Detamornrat, J. Domínguez-Robles, R. F. Donnelly, K. De Wael, *Talanta* **2022**, *249*, 123695.
[29] S. A. Ranamukhaarachchi, C. Padeste, U. O. Hafeli, B. Stoeber, V. J. Cadarso, *J. Micromech. Microeng.* **2017**, *28*, 024002.
[30] D. Han, R. S. Morde, S. Mariani, A. A. La Mattina, E. Vignali, C. Yang, G. Barillaro, H. Lee, *Adv. Funct. Mater.* **2020**, *30*, 1909197.
[31] L. Barnum, J. Quint, H. Derakhshandeh, M. Samandari, F. Aghabaglou, A. Farzin, L. Abbasi, S. Bencherif, A. Memic, P. Mostafalu, A. Tamayol, *Adv. Healthcare Mater.* **2021**, *10*, 2001922.
[32] Z. Faraji Rad, P. D. Prewett, G. J. Davies, *Microsyst. Nanoeng.* **2021**, *7*, 71.
[33] Z. Faraji Rad, R. E. Nordon, C. J. Anthony, L. Bilston, P. D. Prewett, J.-Y. Arns, C. H. Arns, L. Zhang, G. J. Davies, *Microsyst. Nanoeng.* **2017**, *3*, 1.
[34] Á. Cárcamo-Martínez, B. Mallon, J. Domínguez-Robles, L. K. Vora, Q. K. Anjani, R. F. Donnelly, *Int. J. Pharm.* **2021**, *599*, 120455.
[35] Z. Chen, H. Wu, S. Zhao, X. Chen, T. Wei, H. Peng, Z. Chen, *Mol. Pharmaceutics* **2022**, *19*, 3314.
[36] Y. Liu, Q. Yu, X. Luo, L. Yang, Y. Cui, *Microsyst. Nanoeng.* **2021**, *7*, 75.
[37] Y. Li, H. Zhang, R. Yang, Y. Laffitte, U. Schmill, W. Hu, M. Kaddoura, E. J. M. Blondeel, B. Cui, *Microsyst. Nanoeng.* **2019**, *5*, 41.
[38] M. Dervisevic, E. Dervisevic, L. Esser, C. D. Easton, V. J. Cadarso, N. H. Voelcker, *Biosens. Bioelectron.* **2023**, *222*, 114955.
[39] S. P. Davis, B. J. Landis, Z. H. Adams, M. G. Allen, M. R. Prausnitz, *J. Biomech.* **2004**, *37*, 1155.
[40] M. R. Prausnitz, *Adv. Drug Delivery Rev.* **2004**, *56*, 581.
[41] L. Lin, Y. Wang, M. Cai, X. Jiang, Y. Hu, Z. Dong, D. Yin, Y. Liu, S. Yang, Z. Liu, J. Zhuang, Y. Xu, C. Fei Guo, L. Chang, *Adv. Funct. Mater.* **2022**, *32*, 2109187.
[42] U. Detamornrat, E. Mcalister, A. R. J. Hutton, E. Larrañeta, R. F. Donnelly, *Small* **2022**, 2106392.
[43] C. Kolluru, M. Williams, J. Chae, M. R. Prausnitz, *Adv. Healthcare Mater.* **2019**, *8*, 1801262.
[44] P. P. Samant, M. R. Prausnitz, *Proc. Natl. Acad. Sci.* **2018**, *115*, 4583.
[45] M. Dervisevic, M. Alba, B. Prieto-Simon, N. H. Voelcker, *Nano Today* **2020**, *30*, 100828.
[46] S. M. Laville, A. Couturier, O. Lambert, M. Metzger, N. Mansencal, C. Jacquelinet, M. Laville, L. Frimat, D. Fouque, *Nephrol. Dial. Transplant.* **2023**, *38*, 184.
[47] Y. Marunaka, *World J. Diabetes* **2015**, *6*, 125.
[48] W. Aoi, Y. Marunaka, *Biomed Res. Int.* **2014**, *2014*, 598986.
[49] K. H. Steen, A. E. Steen, P. W. Reeh, *J. Neurosci.* **1995**, *15*, 3982.
[50] J. Dissemond, M. Witthoff, T. C. Brauns, D. Haberer, M. Goos, *Hautarzt* **2003**, *54*, 959.
[51] M. Dervisevic, M. J. Jara Fornerod, J. Harberts, P. S. Zangabad, N. H. Voelcker, *ACS Sens.* **2024**, *9*, 932.
[52] W. O. Ho, S. Krause, C. J. McNeil, J. A. Pritchard, R. D. Armstrong, D. Athey, K. Rawson, *Anal. Chem.* **1999**, *71*, 1940.
[53] L. Liu, H. Mo, S. Wei, D. Raftery, *Analyst* **2012**, *137*, 595.
[54] M. Czauderna, J. Kowalczyk, *Czech J. Anim. Sci.* **2012**, *57*, 19.
[55] H. Ray, D. Saetta, T. H. Boyer, *Environ. Sci. Water Res. Technol.* **2018**, *4*, 87.
[56] M. Fidaleo, R. Lavecchia, *Chem. Biochem. Eng. Q.* **2003**, *17*, 311.
[57] A. H. Bretag, *Life Sci.* **1969**, *8*, 319.
[58] Y. Zhang, H. Guo, S. B. Kim, Y. Wu, D. Ostojich, S. H. Park, X. Wang, Z. Weng, R. Li, A. J. Bandodkar, Y. Sekine, J. Choi, S. Xu, S. Quaggin, R. Ghaffari, J. A. Rogers, *Lab Chip* **2019**, *19*, 1545.

© 2025 The Author(s). Advanced Materials Technologies published by Wiley-VCH GmbH

2365709x, 2025, 22, Downloaded from https://advanced.onlinelibrary.wiley.com/doi/10.1002/admt.202500891 by Koc University, Wiley Online Library on [07/12/2025]. See the Terms and Conditions (https://onlinelibrary.wiley.com/terms-and-conditions) on Wiley Online Library for rules of use; OA articles are governed by the applicable Creative Commons License